Monthly Notices of the ROYAL ASTRONOMICAL SOCIETY

MNRAS **522,** 4565–4576 (2023) https://doi.org/10.1093/mnras/stad1269
Advance Access publication 2023 April 28

Generalized equipartition method from an arbitrary viewing angle

Tatsuya Matsumoto[1]★ and Tsvi Piran[2]

[1]*Department of Physics and Columbia Astrophysics Laboratory, Columbia University, Pupin Hall, New York, NY 10027, USA*
[2]*Racah Institute of Physics, Hebrew University, Jerusalem 91904, Israel*

Accepted 2023 April 25. Received 2023 April 25; in original form 2022 November 18

ABSTRACT

The equipartition analysis yields estimates of the radius and energy of synchrotron self-absorbed radio sources. Here we generalize this method to relativistic off-axis viewed emitters. We find that the Lorentz factor Γ and the viewing angle θ cannot be determined independently but become degenerate along a trajectory of minimal energy solutions. The solutions are divided into on-axis and off-axis branches, with the former reproducing the classical analysis. A relativistic source viewed off-axis can be disguised as an apparent Newtonian one. Applying this method to radio observations of several tidal disruption events, we find that the radio flare of AT 2018hyz, which was observed a few years after the optical discovery, could have been produced by a relativistic off-axis jet with a kinetic energy of $\sim 10^{53}$ erg that was launched around the time of discovery.

Key words: transients: tidal disruption events.

1 INTRODUCTION

The equipartition method gives estimates of the radius and energy of a radio source showing a synchrotron self-absorbed spectrum (Pacholczyk 1970; Scott & Readhead 1977; Chevalier 1998; Barniol Duran, Nakar & Piran 2013, hereafter BNP13; see also e.g. Zdziarski 2014; Petropoulou & Dermer 2016 for the case without self-absorption). This method is based on the fact that the total energy of the emitting non-thermal electrons and magnetic field has a very narrow minimum as a function of the outflow's radius. At the minimum, both energies are comparable, and even a tiny deviation from the radius significantly increases the energy. While the original equipartition method applies to only non-relativistic radio sources, BNP13 extended it for relativistic sources moving toward an observer (on-axis emitter). Here we define the 'on-axis' configuration in which the observer is located within the beaming cone whose half-opening angle is given by $\theta_{\rm b} \simeq 1/\Gamma$ of the source. Their extended analysis has been applied to bright radio sources likely powered by a relativistic jet in tidal disruption events (TDEs; Barniol Duran & Piran 2013; Eftekhari et al. 2018).

When a radio source is a relativistic and collimated outflow, like a jet, its appearance drastically varies depending on a viewing angle. In particular, the outflow travels in a different direction from an observer's line of sight. Initially, the emission is strongly suppressed to the observer because of the relativistic de-beaming effect. As discussed for gamma-ray bursts (GRBs; Granot et al. 2002; Rossi, Lazzati & Rees 2002; Totani & Panaitescu 2002), the light curve peaks at a later time when the jet decelerates, and the observer enters its beaming cone (becoming from off- to on-axis). This naturally explains the afterglow light curve of GRB 170817A, which we observed at $\simeq 0.2$ rad from the jet axis (e.g. see Margutti & Chornock 2021, and references therein).

More recently, radio follow-ups for optical TDEs have revealed delayed radio flares (Horesh, Cenko & Arcavi 2021a; Horesh et al. 2021b; Cendes et al. 2022; Perlman et al. 2022; Sfaradi et al. 2022). In contrast to typical radio flares following optical TDEs (Alexander et al. 2020), these delayed events appear a few years after the optical discovery, and some of them are still in a brightening phase (Horesh et al. 2021a; Cendes et al. 2022). One of the possible origins of the delayed radio flares is an off-axis jet. However, previous analyses were carried out in the assumption of the Newtonian or on-axis case and cannot discuss the possibility of the off-axis jet scenario.

Motivated by the recent detection of delayed radio flares in TDEs, we further extend the equipartition method for an arbitrary viewing angle, i.e. both on- and off-axis cases. This paper is organized as follows: In Section 2, the equipartition method of BNP13 is generalized for arbitrary viewing angle observers. Using the generalized analysis, we develop a new formalism in Section 3 and apply it to several TDEs whose radio signals are possibly produced by off-axis emission in Section 4. Finally, we summarize the method and our findings in Section 5.

2 GENERALIZATION OF EQUIPARTITION METHOD

Consider a relativistically moving radio source with a Lorentz factor Γ. The source is at a distance R from the centre of an explosion. An observer whose line of sight has an angle of θ from the source's direction of motion detects its radio-synchrotron emission characterized by a peak frequency $\nu_{\rm p}$ and flux density $F_{\rm p}$ (see Fig. 1). The relativistic radio source could have an angular structure (i.e. the Lorentz factor and energy vary for different angles). However, due to the strong dependence of the beaming on the Lorentz factor, a small region of order π/Γ^2, dominates the observed emission. Therefore, the radio emission site can be characterized by a single Lorentz factor and regarded as a small patch (Ioka & Nakamura 2019; Matsumoto, Nakar & Piran 2019a,b).

★ E-mail: tm3238@columbia.edu

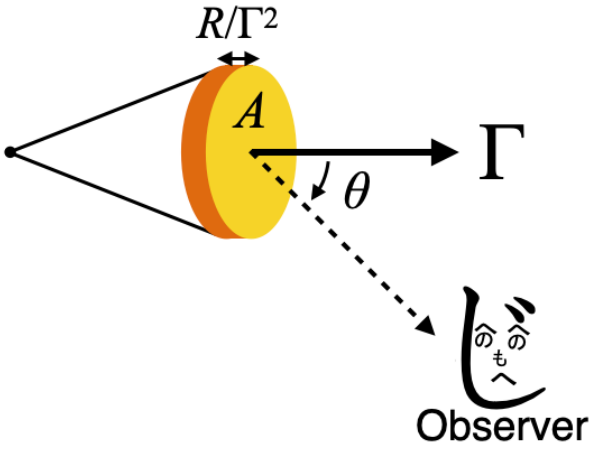

Figure 1. A schematic picture. A radio-emitting region is moving at a Lorentz factor Γ whose direction of motion is away from the observer's line of sight, θ. The emitting region has an emitting area A and volume of V.

The observed quantities are translated from the quantities in the rest frame via the relativistic Doppler factor:

$$\delta_{\rm D} = \frac{1}{\Gamma\left(1-\beta\cos\theta\right)} , \tag{1}$$

where $\beta \equiv \sqrt{1-1/\Gamma^2}$ is the source velocity normalized by the speed of light c. Note that for a source moving precisely towards the observer ($\theta = 0$), the Doppler factor becomes $\delta_{\rm D} = 2\Gamma$. However, BNP13 (following Sari, Piran & Narayan 1998) approximated it as $\delta_{\rm D} \simeq \Gamma$ to reflect the fact that the average $\delta_{\rm D}$ is lower than 2Γ.[1] In this paper, we use an exact value of $\delta_{\rm D}$ for a given angle to see the off-axis effect. This treatment leads to some differences in numerical factors between our results at the limit of $\theta = 0$ and those of BNP13.[2]

The observed peak frequency is given by the Doppler-boosted (and redshifted) synchrotron frequency:

$$\nu_{\rm p} = \frac{\delta_{\rm D} q_{\rm e} B \gamma_{\rm e}^2}{2\pi m_{\rm e} c (1+z)} , \tag{2}$$

where $q_{\rm e}$ is the elementary charge, B is the magnetic field (at the source rest frame), $\gamma_{\rm e}$ is the Lorentz factor of electrons producing the radio peak, $m_{\rm e}$ is the electron mass, and z is the redshift to the source.

Two expressions give the peak flux density for optically thin and thick regimes (we describe a more detailed derivation in Appendix A). In the optically thin regime,[3] the flux density is just given by the flux of a single electron with the Lorentz factor $\gamma_{\rm e}$ multiplied by the number of emitting electrons $N_{\rm e}$:

$$F_{\rm p} = \frac{(1+z)\delta_{\rm D}^3 \sqrt{3} q_{\rm e}^3 B N_{\rm e}}{4\pi d_{\rm L}^2 m_{\rm e} c^2} , \tag{3}$$

where $d_{\rm L}$ is the luminosity distance to the source. We estimate the peak flux by the self-absorbed spectrum in the optically thick regime. There are potentially two cases depending on the ratio between self-absorption frequency $\nu_{\rm a}$ and the characteristic synchrotron frequency $\nu_{\rm m}$ (corresponding to the emitting electrons with the least energy; see e.g. Sari et al. 1998). In the case of $\nu_{\rm a} > \nu_{\rm m}$, the flux at $\nu_{\rm m}$ is suppressed by self-absorption and the radio flux peaks at $\nu_{\rm a}$. The peak flux is given by the Rayleigh–Jeans spectrum:

$$F_{\rm p} \simeq \frac{(1+z)^3 \delta_{\rm D} 2 m_{\rm e} \gamma_{\rm e} \nu_{\rm p}^2 A}{d_{\rm L}^2} , \tag{4}$$

where A is the surface area of the emitting region. In the opposite case of $\nu_{\rm m} > \nu_{\rm a}$, the flux peaks at $\nu_{\rm m}$ which is obtained by extending the self-absorbed spectrum:

$$F_{\rm p} \simeq \frac{(1+z)^3 \delta_{\rm D} 2 m_{\rm e} \gamma_{\rm e} \nu_{\rm a}^2 A}{d_{\rm L}^2} \left(\frac{\nu_{\rm p}}{\nu_{\rm a}}\right)^{1/3} . \tag{5}$$

Combining the two cases, the peak flux is given by

$$F_{\rm p} = \frac{(1+z)^3 \delta_{\rm D} 2 m_{\rm e} \gamma_{\rm e} \nu_{\rm p}^2 A}{3 d_{\rm L}^2} \eta^{1/3} , \tag{6}$$

$$\eta \equiv \begin{cases} 1 & ; \nu_{\rm a} > \nu_{\rm m} , \\ \nu_{\rm m}/\nu_{\rm a} & ; \nu_{\rm a} < \nu_{\rm m} , \end{cases} \tag{7}$$

where following BDP13 we introduced a numerical factor 3 in the denominator of equation (6).

We solve equations (2), (3), and (6) to obtain $\gamma_{\rm e}$, $N_{\rm e}$, and B:

$$\gamma_{\rm e} = \frac{3 F_{\rm p} d_{\rm L}^2 \eta^{5/3} \Gamma^2}{2\pi \nu_{\rm p}^2 (1+z)^3 m_{\rm e} f_{\rm A} R^2 \delta_{\rm D}}$$
$$\simeq 5.2\times 10^2 \left[\frac{F_{\rm p,mJy} d_{\rm L,28}^2 \eta^{5/3}}{\nu_{\rm p,10}(1+z)^3}\right] \frac{\Gamma^2}{f_{\rm A} R_{17}^2 \delta_{\rm D}} , \tag{8}$$

$$N_{\rm e} = \frac{9 c F_{\rm p}^3 d_{\rm L}^6 \eta^{10/3} \Gamma^4}{2\sqrt{3}\pi^2 q_{\rm e}^2 m_{\rm e}^2 \nu_{\rm p}^5 (1+z)^8 f_{\rm A}^2 R^4 \delta_{\rm D}^4}$$
$$\simeq 4.1\times 10^{54} \left[\frac{F_{\rm p,mJy}^3 d_{\rm L,28}^6 \eta^{10/3}}{\nu_{\rm p,10}^5 (1+z)^8}\right] \frac{\Gamma^4}{f_{\rm A}^2 R_{17}^4 \delta_{\rm D}^4} , \tag{9}$$

$$B = \frac{8\pi^3 m_{\rm e}^3 c \nu_{\rm p}^5 (1+z)^7 f_{\rm A}^2 R^4 \delta_{\rm D}}{9 q_{\rm e} F_{\rm p}^2 d_{\rm L}^4 \eta^{10/3} \Gamma^4}$$
$$\simeq 1.3\times 10^{-2}\,{\rm G} \left[\frac{\nu_{\rm p,10}^5 (1+z)^7}{F_{\rm p,mJy}^2 d_{\rm L,28}^4 \eta^{10/3}}\right] \frac{f_{\rm A}^2 R_{17}^4 \delta_{\rm D}}{\Gamma^4} , \tag{10}$$

where we use the convention $Q_{\rm x} = Q/10^{\rm x}$ (cgs) except for the flux density $F_{\rm p,mJy} = F_{\rm p}/{\rm mJy}$. The emitting area is measured in units of a surface area of a sphere with a radius R, subtending a solid angle of π/Γ^2. We define an area-filling factor following BNP13:

$$f_{\rm A} \equiv A/\left(\pi R^2/\Gamma^2\right) . \tag{11}$$

A volume-filling factor is also defined by measuring the emitting volume in units of a typical volume of a relativistic shell, i.e. a shell with a radius R, width R/Γ^2, and solid angle of π/Γ^2:

$$f_{\rm V} = V/\left(\pi R^3/\Gamma^4\right) . \tag{12}$$

[1] Averaging the Doppler factor over the beaming cone gives $\langle\delta_{\rm D}\rangle = \int_0^{1/\Gamma} {\rm d}\theta \sin\theta \delta_{\rm D}/(1-\cos\theta) \simeq (2\ln 2)\,\Gamma \simeq 1.4\,\Gamma$ for $\Gamma \gg 1$ and $\theta \ll 1$.

[2] The exact differences between our equations and those of BNP13 are summarized as follows: equations (2), (3), (6), and (10) are twice larger than corresponding equations (10), (11), (13), and (16) of BNP13 in the limit of $\theta = 0$. Equation (8) is twice smaller than equation (14), equation (9) is four times smaller than equation (15), equation (14) is eight times smaller than equation (17), and equation (15) is four times larger than equation (18) of BNP13.

[3] Throughout this paper, we assume that the emission is produced by non-thermal electrons with a power-law energy distribution (${\rm d}n/{\rm d}\gamma \propto \gamma^{-p}$) in a single zone. Therefore, the spectral index in the optically thin regime should be smaller than -0.5 so that the power-law index is $p > 2$.

These definitions of filling factors[4] are useful and relevant for the emitting source at a radius R from the explosion centre moving at a Lorentz factor Γ. In Appendix B, we discuss the case in which the outflow has a fixed half-opening angle θ_j and hence $f_A = f_V = (\Gamma\theta_j)^2$.

Once the number of electrons is obtained (equation 9), we estimate the number density of the circumnuclear medium (CNM):

$$n_e \simeq \frac{N_e}{\frac{\Omega}{3}R^3} = \frac{27cF_p^3 d_L^6 \eta^{10/3}\Gamma^4}{2\sqrt{3}\pi^3 q_e^2 m_e^2 \nu_p^5 (1+z)^8 f_A^2 f_\Omega R^4 \delta_D^4}$$
$$\simeq 3.9\times10^3\,\mathrm{cm}^{-3}\left[\frac{F_{p,mJy}^3 d_{L,28}^6 \eta^{10/3}}{\nu_{p,10}^5 (1+z)^8}\right]\frac{\Gamma^6}{f_A^2 f_\Omega R_{17}^7 \delta_D^4}\,, \quad (13)$$

where Ω is the solid angle subtended by the outflow, and we define the filling factor $f_\Omega \equiv \Omega/(\pi/\Gamma^2)$ following equations (11) and (12). Note this number density is a lower limit because all electrons are assumed to be accelerated to relativistic energies (e.g. see Matsumoto & Piran 2021).

The emitting electron's energy and the magnetic field's energy in the lab frame are calculated by

$$E_e = m_e c^2 \gamma_e \Gamma N_e = \frac{27c^3 F_p^4 d_L^8 \eta^5 \Gamma^7}{4\sqrt{3}\pi^3 q_e^2 m_e^2 \nu_p^7 (1+z)^{11} f_A^3 R^6 \delta_D^5}$$
$$\simeq 1.8\times10^{51}\,\mathrm{erg}\left[\frac{F_{p,mJy}^4 d_{L,28}^8 \eta^5}{\nu_{p,10}^7 (1+z)^{11}}\right]\frac{\Gamma^7}{f_A^3 R_{17}^6 \delta_D^5}\,, \quad (14)$$

$$E_B = \frac{B^2}{8\pi}\Gamma^2 V = \frac{8\pi^6 m_e^6 c^2 \nu_p^{10} (1+z)^{14} f_A^4 f_V R^{11} \delta_D^2}{81 q_e^2 F_p^4 d_L^8 \eta^{20/3}\Gamma^{10}}$$
$$\simeq 6.8\times10^{45}\,\mathrm{erg}\left[\frac{\nu_{p,10}^{10}(1+z)^{14}}{F_{p,mJy}^4 d_{L,28}^8 \eta^{20/3}}\right]\frac{f_A^4 f_V R_{17}^{11}\delta_D^2}{\Gamma^{10}}\,. \quad (15)$$

The total energy of the emitting electrons and the magnetic field is

$$E_{tot} = E_e + E_B = E_{eq}\left[\frac{11}{17}\left(\frac{R}{R_{eq}}\right)^{-6} + \frac{6}{17}\left(\frac{R}{R_{eq}}\right)^{11}\right], \quad (16)$$

where

$$R_{eq} \equiv R_{eq,N}\Gamma\delta_D^{-7/17}\,, \quad (17)$$

$$R_{eq,N} \equiv \left(\frac{3^8 c F_p^8 d_L^{16}\eta^{35/3}}{2^4 11\sqrt{3}\pi^9 m_e^8 \nu_p^{17}(1+z)^{25} f_A^7 f_V}\right)^{1/17}$$
$$\simeq 1.9\times10^{17}\,\mathrm{cm}\left[\frac{F_{p,mJy}^{\frac{8}{17}} d_{L,28}^{\frac{16}{17}}\eta^{\frac{35}{51}}}{\nu_{p,10}(1+z)^{\frac{25}{17}}}\right] f_A^{-\frac{7}{17}} f_V^{-\frac{1}{17}}\,, \quad (18)$$

and

$$E_{eq} = E_{eq,N}\Gamma\delta_D^{-43/17}\,, \quad (19)$$

$$E_{eq,N} \equiv \left(\frac{17^{17}\pi^3 c^{45} m_e^{14} F_p^{20} d_L^{40}\eta^{15} f_V^6}{2^{10}3^2 11^{11}\sqrt{3} q_e^{34}\nu_p^{17}(1+z)^{37} f_A^9}\right)^{1/17}$$
$$\simeq 6.2\times10^{49}\,\mathrm{erg}\left[\frac{F_{p,mJy}^{\frac{20}{17}} d_{L,28}^{\frac{40}{17}}\eta^{\frac{15}{17}}}{\nu_{p,10}(1+z)^{\frac{37}{17}}}\right] f_A^{-\frac{9}{17}} f_V^{\frac{6}{17}}\,. \quad (20)$$

Here, we factored out the relativistic corrections in equations (17) and (19) and define the Newtonian equipartition radius and energy by equations (18) and (20), which are determined by the observables and the geometrical parameters f_A and f_V.

[4]While BNP13 originally introduced these geometrical factors for the relativistic case, they turned out to be significant in the Newtonian case as well (Yalinewich et al. 2019; Matsumoto & Piran 2021).

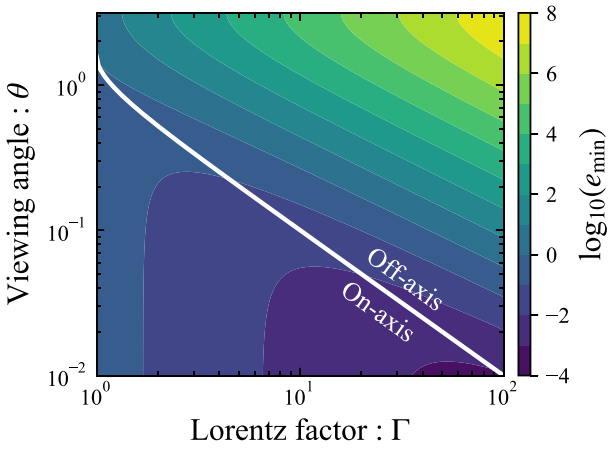

Figure 2. The distribution of the minimal normalized energy (equation 23) for different Lorentz factors and viewing angles. The on- and off-axis regions are divided by the white line $\theta \simeq 1/\Gamma$ (see equation 25). For given observations, the energy is smaller for on-axis observers than off-axis ones, and its value decreases for larger Lorentz factors.

We emphasize that the total energy in equation (16) contains only emitting electrons and magnetic field energies. The contribution of non-emitting electrons and baryons increases the energy. We refer the readers to BNP13 for such extensions. However, these corrections do not change the qualitative nature of the solution.

Normalizing the variables to the Newtonian quantities, we define

$$r \equiv R/R_{eq,N} \quad \text{and} \quad e \equiv E/E_{eq,N}, \quad (21)$$

and now rewrite equation (16) as:

$$e(r,\Gamma,\theta) = \Gamma\delta_D^{-43/17}\left[\frac{11}{17}\left(\frac{r}{\Gamma\delta_D^{-7/17}}\right)^{-6} + \frac{6}{17}\left(\frac{r}{\Gamma\delta_D^{-7/17}}\right)^{11}\right]. \quad (22)$$

The relativistic effects are now seen clearly in the appearance of Γ and δ_D. Note, however, that they also appear indirectly in the definitions of geometrical factors f_A and f_V.

3 MINIMAL ENERGY

In the Newtonian equipartition analysis ($\Gamma = 1$ and $\delta_D = 1$), the total energy depends only on the radius, and it is minimized at $R_{eq,N}$. As is well-known, a slight deviation from $R_{eq,N}$ increases the total energy by orders of magnitude, and hence the actual radius is $\approx R \simeq R_{eq,N}$ and the energy is not much larger than $E \simeq E_{eq,N}$. In contrast, for the relativistic regime, with the additional two variables Γ and θ, the energy no longer has a global minimum. An additional consideration is required to determine the radius and energy.

Still, even in the relativistic case, the energy has a very sharp minimum as a function of r,

$$e_{min}(\Gamma,\theta) = \Gamma\delta_D^{-43/17}\,, \quad (23)$$

at

$$r = \Gamma\delta_D^{-7/17}\,. \quad (24)$$

Fig. 2 depicts the minimal energy e_{min} as a function of Γ and θ. For a fixed Lorentz factor, the energy is always minimized for an exactly

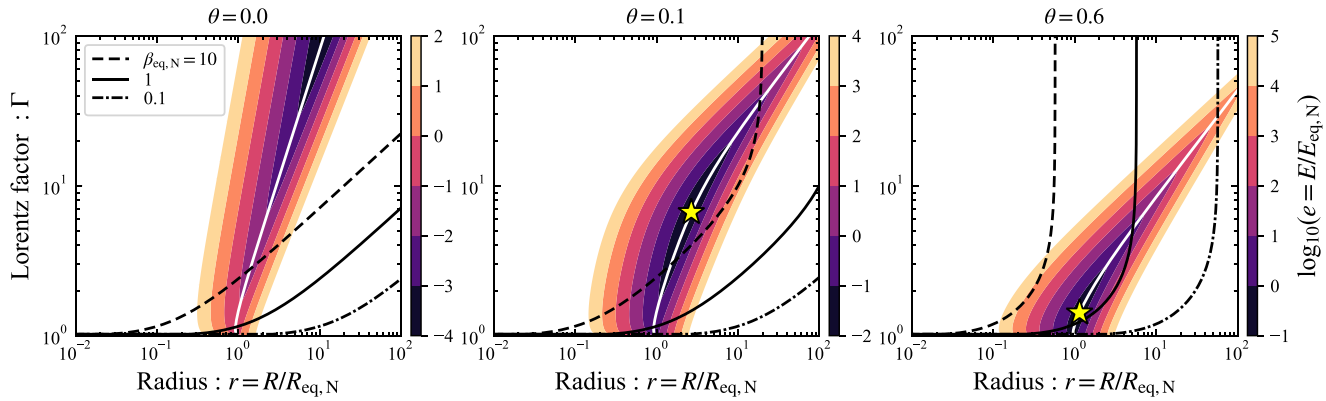

Figure 3. Distributions of the total energy (equation 22) as a function of radius and Lorentz factor for different viewing angles of $\theta = 0$, 0.1, and 0.6 (left to right). White curves represent the radius minimizing the energy for each Lorentz factor and angle (equation 27). Black curves show the contours for fixed $\beta_{\rm eq,N} = R_{\rm eq,N}(1+z)/(ct) = 10$ (dashed), 1 (solid), and 0.1 (dash–dotted). For the middle and right-hand panels, star points denote the location where the energy is minimized for the given angle.

on-axis configuration ($\theta = 0$), and it does not vary so much as long as the emission is viewed from on-axis $\theta < 1/\Gamma$. In other words, off-axis sources require more energy than on-axis ones, and the energy increases by many orders of magnitude as θ increases. For an on-axis observer, the minimal energy decreases quickly, $e_{\rm min} \propto \Gamma^{-26/17}$, as the source becomes more relativistic (BNP13, and see the left-hand panel of Fig. 3). For a fixed viewing angle, the energy has a minimum around the boundary between the on- and off-axis.

The behaviour of $e_{\rm min}$ is explained by the fact that the emission is amplified by the substantial Doppler boost, and less energy is needed to produce a given observed flux. Note that the geometrical factors $f_{\rm A}$ and $f_{\rm V}$ are assumed to be constant here. Namely, the actual physical size of the emitting region decreases for larger Γ, which also helps to reduce the minimal energy.[5] Regardless of this unphysical assumption of a highly narrow emitter moving at an extremely large Lorentz factor, this result implies that unlike the Newtonian case, there is no global minimum for the energy of the source, and other considerations have to be added to determine the conditions at the source entirely.

The definition of on (off) axis, $\theta < (>) 1/\Gamma$ becomes irrelevant for Newtonian sources because $\Gamma \to 1$ results in $\theta = 1$ as the boundary between the on- and off-axis. This is not true because an emission from the source can be seen from any angle. Here, for completeness, we define the size of the beaming cone by an angle within which half of the photons are isotropically emitted in the source rest frame is confined in the lab frame. With this definition, the beaming cone is given by

$$\theta_{\rm b} = \cos^{-1}\beta\ , \tag{25}$$

which asymptotes to $\theta_{\rm b} \to 1/\Gamma$ for $\Gamma \gg 1$ restoring the conventional definition of the beaming angle. Hereafter, we use this definition to depict the boundary between on- and off-axes in figures.

Fig. 3 depicts the distribution of the normalized energy, $e(r, \Gamma,$ and $\theta)$ (equation 22) in the (r, Γ) plane for different viewing angles. As a function of r, the energy takes a minimal value for $r = \Gamma\delta_{\rm D}^{-7/17}$ (white curve on each panel). As we have already seen that in the relativistic case, due to the additional dependence on Γ and θ, the energy (equation 22) no longer has a global minimum. Indeed for $\theta = 0$ (the left-hand panel in Fig. 3), the energy e is arbitrarily decreased by increasing Γ. For finite angles, $\theta \neq 0$, the energy has a minimal value at a point on $r = \Gamma\delta_{\rm D}^{-7/17}$ (stars in the middle and right-hand panels in Fig. 3). However, the variation of the total energy along the trajectory of $r = \Gamma\delta_{\rm D}^{-7/17}$ is much milder than the case in which r deviates from $\Gamma\delta_{\rm D}^{-7/17}$. Therefore, even for a finite angle case, requiring minimal energy, as in the Newtonian case, is insufficient in the relativistic case.

Following BNP13 we introduce an additional condition on the three variables. When the moment of the explosion (or equivalently, the launch of the outflow) is observationally identified, the radius and the observation time t (measured since the explosion in the observer frame) are related by

$$t = \frac{(1+z)R}{c\beta}(1 - \beta\cos\theta)\ . \tag{26}$$

This gives a second relation between the three variables:

$$r = \left(\frac{\beta}{\beta_{\rm eq,N}}\right)\Gamma\delta_{\rm D}\ , \tag{27}$$

$$\beta_{\rm eq,N} \equiv \frac{(1+z)R_{\rm eq,N}}{ct} \simeq 0.73\left[\frac{F_{\rm p,mJy}^{\frac{8}{17}} d_{\rm L,28}^{\frac{16}{17}} \eta^{\frac{35}{51}}}{\nu_{\rm p,10}(1+z)^{\frac{8}{17}}}\left(\frac{t}{100\,{\rm d}}\right)^{-1}\right] f_{\rm A}^{-7/17} f_{\rm V}^{-1/17}\ . \tag{28}$$

The parameter $\beta_{\rm eq,N}$ describes an apparent velocity of the emitting source. Notably, $\beta_{\rm eq,N} < 1$ suggests that the source is Newtonian. However, we will show this is not necessarily the case.

Black lines in Fig. 3 show contours of equation (27) for $\beta_{\rm eq,N} = 10$, 1, and 0.1. The radius and the Lorentz factor are restricted along a curve for a given $\beta_{\rm eq,N}$ by an observation (with fixed geometrical parameters $f_{\rm A}$ and $f_{\rm V}$). For $\theta = 0$, this curve always intersects the curve of $r = \Gamma\delta_{\rm D}^{-7/17}$ at a single point, which gives a unique estimate of the radius and corresponding Lorentz factor (BNP13). In contrast, these curves may intersect twice or never for $\theta \neq 0$. This is because equation (27) asymptotes to $r \simeq 2/(\beta_{\rm eq,N}\theta^2)$ for $\Gamma \gtrsim 1/\theta$ (the observed time caps the outflow's radial distance). When there are two intersections, there are two corresponding minimal energies. When there is no intersection, the energy takes a minimum at a smaller radius than $r = \Gamma\delta_{\rm D}^{-7/17}$, and its value is typically much larger than that obtained on this line. Fig. 4 shows the behaviour of

[5]This does not necessarily mean that the whole energy of the explosion is small. Most of the emission from other regions is beamed away and hidden from the observer at this stage.

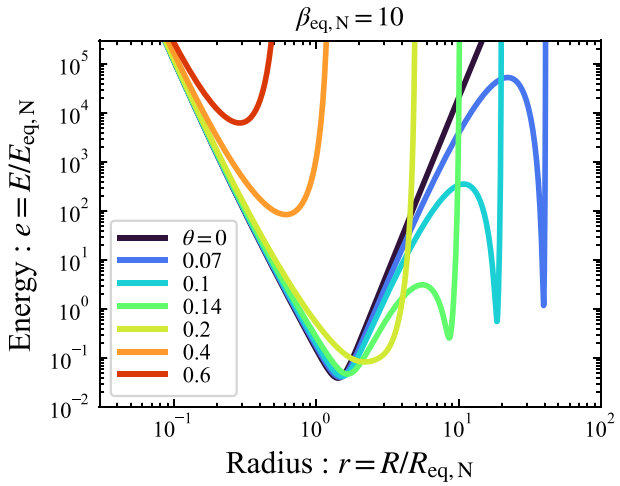

Figure 4. Total energy as a function of radius. This is the variation of energy along black dashed curves (equation 27) in Fig. 3 for different θ. We fix the ratio $\beta_{\rm eq,N}=10$ while different values of $\beta_{\rm eq,N}$ give a similar behaviour qualitatively. For $\theta<\theta_{\rm c}\simeq 0.2$ (equation 37), the energy has two minima corresponding to on (smaller radius) and off-axis (larger radius) solutions.

the energy (equation 22) along the radius given by equation (27) for different viewing angles. For smaller (but non-zero) viewing angles, the energy has two minimal values, as shown in Fig. 3.

For given θ and $\beta_{\rm eq,N}$, we derive the minimal energies and corresponding Lorentz factor and radii, which give the intersections of the white and black curves in Fig. 3. Combining equations (24) and (27), we find the Doppler factor is constrained

$$\delta_{\rm D}=\left(\frac{\beta}{\beta_{\rm eq,N}}\right)^{-17/24}. \tag{29}$$

Given a viewing angle, we solve equation (29) for the Lorentz factor and calculate the corresponding minimal energy and radius:

$$e_{\rm min}=\left(\frac{\beta}{\beta_{\rm eq,N}}\right)^{43/24}\Gamma, \tag{30}$$

$$r=\left(\frac{\beta}{\beta_{\rm eq,N}}\right)^{7/24}\Gamma. \tag{31}$$

In the limit of $\Gamma\gg 1$ and $\theta\ll 1$, we can obtain more explicit results instead of equations (29)–(31). In this limit, the Doppler factor is approximated by

$$\delta_{\rm D}\simeq\frac{2\Gamma}{1+(\Gamma\theta)^2}, \tag{32}$$

and we can rewrite equation (29) as

$$(\Gamma\theta)^2-2\beta_{\rm eq,N}^{-17/24}\Gamma+1\simeq 0. \tag{33}$$

For $\theta=0$, the Lorentz factor and corresponding minimal energy and radius are given by

$$\Gamma_{\rm on}\simeq\frac{\beta_{\rm eq,N}^{17/24}}{2}, \tag{34}$$

$$e_{\rm min,on}\simeq\frac{1}{2\beta_{\rm eq,N}^{13/12}}, \tag{35}$$

$$r_{\rm on}\simeq\frac{\beta_{\rm eq,N}^{5/12}}{2}. \tag{36}$$

These equations are basically the same as those given by BNP13. Here we implicitly assume $\beta_{\rm eq,N}\gtrsim 1$ so that we have $\Gamma_{\rm on}\gtrsim 1$. In the opposite case of $\beta_{\rm eq,N}<1$, we have the same results as the Newtonian equipartition method: $\Gamma_{\rm on}\simeq e_{\rm min,on}\simeq r_{\rm on}\simeq 1$. Equation (33) has no solution when the viewing angle is larger than a critical value,

$$\theta_{\rm c}=\beta_{\rm eq,N}^{-17/24}. \tag{37}$$

For $0<\theta<\theta_{\rm c}$ there are two solutions:

$$\Gamma\simeq\frac{1\pm\sqrt{1-\beta_{\rm eq,N}^{17/12}\theta^2}}{\beta_{\rm eq,N}^{17/24}\theta^2}. \tag{38}$$

The negative sign corresponds to the on-axis solution. It converges to equation (34) in the $\theta\to 0$ limit. The positive sign corresponds to the off-axis configuration.[6] Therefore, this branch is simply described by taking the limit $\Gamma\theta\gg 1$ in equation (33):

$$\Gamma_{\rm off}\simeq\frac{2}{\beta_{\rm eq,N}^{17/24}\theta^2}, \tag{39}$$

$$e_{\rm min,off}\simeq\frac{2}{\beta_{\rm eq,N}^{5/2}\theta^2}, \tag{40}$$

$$r_{\rm off}\simeq\frac{2}{\beta_{\rm eq,N}\theta^2}. \tag{41}$$

The ratios of the Lorentz factors, energies, and radii of on-axis to off-axis solutions are given by:

$$\frac{\Gamma_{\rm on}}{\Gamma_{\rm off}}=\frac{e_{\rm min,on}}{e_{\rm min,off}}=\frac{r_{\rm on}}{r_{\rm off}}=\frac{\beta_{\rm eq,N}^{17/12}\theta^2}{4}=\left(\frac{\theta}{2\theta_{\rm c}}\right)^2<1. \tag{42}$$

where θ is for the off-axis solution. The off-axis branch always has a larger minimal energy and a larger radius than the on-axis ones.

The above equations nicely explain the behaviour of the minimal energies shown in Fig. 4. For $\theta<\theta_{\rm c}\simeq 0.2\,(\beta_{\rm eq,N}/10)^{-17/24}$ (equation 37), the energy has two minima corresponding to the on- and off-axis solutions. The on-axis solution has a lower energy at a smaller radius than the off-axis one. The minimal energy of the on-axis solution is only weakly dependent on the viewing angle. For the off-axis solution, the radius is larger, and the emitter is accordingly more relativistic than the on-axis one. The minimum around this radius is extremely narrow, and a slight deviation from the minimal radius drastically increases the energy. For $\theta>\theta_{\rm c}$, the energy has a single minimal value at a radius smaller than that for $\theta<\theta_{\rm c}$. This is because equations (24) and (27) do not hold at the same time. This minimal value of the energy increases rapidly with θ, and typically it is much larger than $e_{\rm min}$ (or $E_{\rm eq}$).

Fig. 5 depicts the distribution of the normalized energy, $e(r,\,\Gamma,$ and $\theta)$ (equation 22) in the $(\Gamma,\,\theta)$ plane for different $\beta_{\rm eq,N}$ under the condition of equation (27). The locus of the minimal energy is given by equation (29) or approximately described by solving equation (33) for θ:

$$\theta\simeq\left(\frac{2}{\beta_{\rm eq,N}^{17/24}\Gamma}-\frac{1}{\Gamma^2}\right)^{1/2}. \tag{43}$$

As we have discussed, this locus is divided into on- and off-axis branches. The Lorentz factor of the off-axis branch is always larger than that of the on-axis one (see equation 42). Interestingly, a source interpreted as a Newtonian emitter with $\beta_{\rm eq,N}\lesssim 1$ can be a relativistic one viewed off-axis (see also the right-hand panel of Fig. 5). While more energy is required for the relativistic off-axis configuration,

[6]For this solution, $\Gamma\theta>1$ under the condition of equation (37).

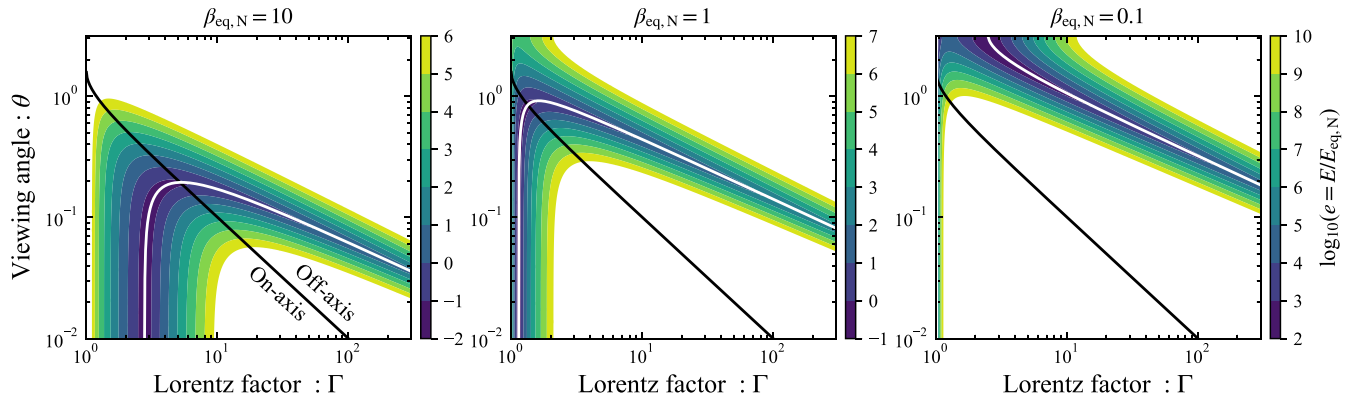

Figure 5. Distributions of the total energy e (equation 22) with the condition of equation (27), as a function of Lorentz factor and viewing angle for different $\beta_{\rm eq,N} = 10$, 1, and 0.1 (left to right). The on- and off-axis regions are divided by the black line $\theta \simeq 1/\Gamma$. White curves give a sequence of minimal energy (equation 29) and possible parameter sets of a radio-emitting source with a given set of observables.

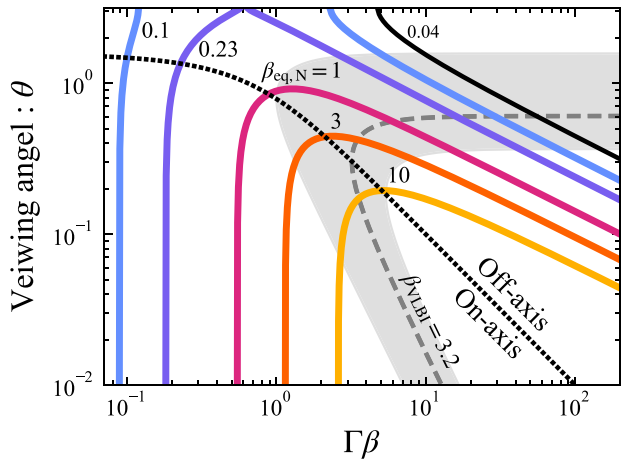

Figure 6. Minimal energy trajectories for different values of $\beta_{\rm eq,N}$ in the ($\Gamma\beta$, θ) plane. For $\beta_{\rm eq,N} < 0.23$, the trajectory has discrete Newtonian (on-axis) and relativistic (off-axis) branches. The grey dashed curve and the coloured stripe around it denote the contour corresponding to an apparent superluminal velocity $\beta_{\rm VLBI} = 3.2 \pm 2.2$. The intersection of a trajectory with the stripe describes a unique solution. The values of $\beta_{\rm VLBI}$ and the black solid curve with $\beta_{\rm eq,N} = 0.04$ correspond to the observations of AT 2019dsg.

there are situations where this is not a problem, and the off-axis solution is the right one.

Fig. 6 shows a sequence of minimal energy trajectories for different values of $\beta_{\rm eq,N}$ in the ($\Gamma\beta$, θ) plane. For a given observation with $\beta_{\rm eq,N}$, the Lorentz factor and viewing angle are not determined independently, but they can vary along this trajectory. As expected, for smaller $\beta_{\rm eq,N}$ values, the on-axis four-velocity approaches the apparent velocity ($\Gamma\beta$) $\rightarrow \beta_{\rm eq,N}$. For small values of $\beta_{\rm eq,N} \lesssim 0.23$, the minimal energy trajectory disappears for $\Gamma\beta \sim 1$, and the trajectory is separated into disconnected Newtonian (on-axis) and relativistic (off-axis) branches. This may be understood by noting the velocity parameter is related to the radio luminosity, $F_{\rm p} d_{\rm L}^2 \propto \beta_{\rm eq,N}^{17/8}$, and hence a smaller $\beta_{\rm eq,N}$ corresponds to a dim source. However, given the strong sensitivity of radio luminosity on the velocity (e.g. Nakar & Piran 2002; Bruni et al. 2021) if $\Gamma\beta \simeq 1$ the source will be too bright and inconsistent with the observed one. A large θ leads to a small Lorentz boost that quenches the observed signal. However, such a solution is strongly off-axis and requires a very large $\Gamma\beta$.

For a single epoch observation that determines $\beta_{\rm eq,N}$, the Lorentz factor and the viewing angle cannot be determined uniquely as there is a degeneracy along the minimal energy trajectory. However, we can break this degeneracy by adding another observational input. Promising information is an apparent velocity obtained by a very long baseline interferometry (VLBI) observation. The displacement of the emitting region on the sky plane gives an apparent speed:

$$\beta_{\rm VLBI} = \frac{\beta \sin\theta}{(1-\beta\cos\theta)(1+z)} \,. \tag{44}$$

In Fig. 6, we show such a trajectory for $\beta_{\rm VLBI} = 3.2$ (motivated by the observation of a TDE; see Section 4.1). It intersects with the minimal energy trajectory, and hence a VLBI observation breaks the degeneracy between Γ and θ.

Since the equipartition method gives both the radius and density (equation 13), it can be used to infer the density profile of galactic nuclear regions (e.g. Barniol Duran & Piran 2013; Zauderer et al. 2013; Alexander et al. 2016; Krolik et al. 2016). For off-axis observers, the outflow radius increases, and the density profile differs from the on-axis one. By equations (13), (24), and (29), we find the density at the minimizing radius depends on the parameters as $n_{\rm e} \propto r^{-1}(\beta/\beta_{\rm eq,N})^{13/12}$. Noting that the velocity becomes $\beta \rightarrow \beta_{\rm eq,N}$ for an on-axis solution with $\beta_{\rm eq,N} < 1$, or $\beta \rightarrow 1$ otherwise, we obtain the ratio of the densities for the off- and on-axis solutions:

$$\frac{n_{\rm off}}{n_{\rm on}} \simeq \max\left[1, \beta_{\rm eq,N}^{-13/12}\right] \left(\frac{r_{\rm off}}{r_{\rm on}}\right)^{-1} \,. \tag{45}$$

4 APPLICATION TO OBSERVED OBJECTS

If the time of the explosion is identified, each observation provides us with the velocity parameter $\beta_{\rm eq,N}$ (equation 28) at each epoch. As the Lorentz factor and the viewing angle are degenerate along the minimal energy trajectory given by equation (29) (see also Fig. 6) we can consider different physical scenarios for the radio source.

Fig. 7 depicts the possible range of $\Gamma\beta$ for each value of $\beta_{\rm eq,N}$. For a given $\beta_{\rm eq,N}$, the four-velocity takes the minimal value at $\theta = 0$. For larger four-velocities, the viewing angle increases up to the critical angle $\theta_{\rm c}$, which typically coincides with the boundary between the on- and off-axis branches for $\beta_{\rm eq,N} \gtrsim 1$, and then it decreases along the off-axis branch. When $\beta_{\rm eq,N}$ is smaller than a critical value $\beta_{\rm eq,N} \lesssim 0.23$, the possible region of $\Gamma\beta$ is separated into relativistic and

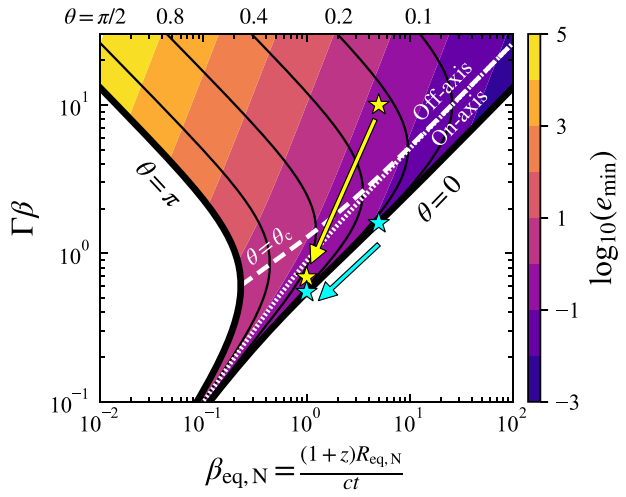

Figure 7. The possible range of four-velocity $\Gamma\beta$ given by the minimal energy trajectory for each $\beta_{\rm eq,N}$. The corresponding viewing angle and minimal energy are shown with black and coloured contours. White dashed and dotted curves denote the contours of the maximal viewing angle ($\theta_{\rm c}$) and the boundary of on- and off-axis configurations ($\theta = \cos^{-1}\beta$). The cyan stars represent the evolution of a decelerating on-axis emitter (the top panel of Fig. 8). The yellow ones show the case of an emitting region evolving from off to on-axis configurations (the bottom panel of Fig. 8).

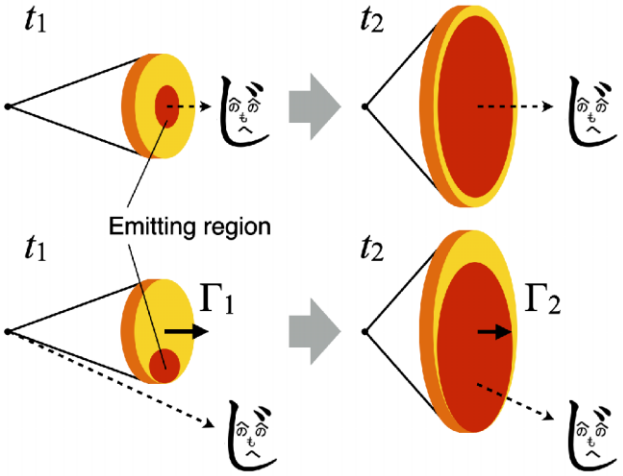

Figure 8. A schematic picture of two temporal evolutions of the radio-emitting region corresponding to the cyan and yellow stars in Fig. 7. (Top) The radio emitter is viewed on-axis from epochs t_1 to t_2 as the emitting region decelerates from Γ_1 to Γ_2. The observer's line of sight coincides with the emitter's direction of motion. (Bottom) The emitter evolves from off to on-axis configurations. The observer is out of the beaming cone at t_1 but enters the cone as the radio source decelerates.

Newtonian regions. In the Newtonian region, the solution is naturally on-axis, and the velocity converges to $\Gamma\beta \rightarrow \beta_{\rm eq,N}$.

We consider observations at two epochs t_1 and t_2 measured from the time of the explosion ($t_1 < t_2$). As an example, let us consider the case in which the apparent velocity parameter $\beta_{\rm eq,N}$ decreases with time [$\beta_{\rm eq,N}(t_1) > \beta_{\rm eq,N}(t_2)$]. Two possible evolutions of the radio source are shown in Fig. 7. One is an on-axis viewed emitter (cyan stars along the contour of $\theta = 0$). The emitting region is moving along the observer's line of sight (as assumed in BNP13). The other is an emitting region evolving from off-axis to on-axis (yellow stars). This is the case when a relativistic jet is launched in a different direction from an observer's line of sight. Initially, only a small fraction of the jet closer to the line of sight (or 'jet's wing' if it has an angular structure) dominates the emission. Then, as the jet decelerates, the observer can see the whole jet in an on-axis configuration. In this case, the equipartition energy, which reflects just the energy of the observed region, increases with time as the jet slows down and a larger fraction of the jet comes into view and contributes to the emission. The corresponding schematic pictures for both situations are shown in the top (on-axis) and the bottom (off- to on-axis) panels of Fig. 8.

We turn now to apply our generalized equipartition method to observed objects. We focus on radio emissions from TDEs. A fraction of TDEs is accompanied by a radio flare with a synchrotron self-absorbed spectrum, which is analysed using the equipartition method (see Alexander et al. 2020, for a review). In the following, we analyse, as an example, two TDEs.

4.1 AT 2019dsg

First, we demonstrate applying the generalized equipartition method to a well-observed event AT 2019dsg (Lee et al. 2020; Cannizzaro et al. 2021; Cendes et al. 2021; Stein et al. 2021; Mohan et al. 2022). It has been suggested that AT 2019dsg was associated with a high-energy neutrino (Stein et al. 2021).

Previous on-axis equipartition analyses found that the observations are consistent with a Newtonian outflow with $\beta \sim 0.1$ launched 10 d before the optical discovery (Cendes et al. 2021; Matsumoto, Piran & Krolik 2022). The energy implied was modest of order $\simeq 10^{47}$ erg. In contrast to these results, some theoretical models for the neutrino emission require a relativistic and more energetic outflow (e.g. Winter & Lunardini 2021), which can be tested by our analysis.

The top panel of Fig. 9 depicts the evolution of the parameter $\beta_{\rm eq,N}$ (data are taken from Cendes et al. 2021). We set the time of the outflow launch as 10 d before the optical discovery, as found by previous analyses. Since $\beta_{\rm eq,N} \simeq 0.04 < 0.23$, the possible range of $\Gamma\beta$ has two branches: Newtonian and relativistic velocities. We derive a possible range of four-velocities for each observation epoch, equipartition radii, and energies (shown in the bottom panels of Fig. 9). Although the viewing angle has a range of $0 \leq \theta \leq \pi$, we show the colour contours only up to $\theta \lesssim \pi/2$ [note $\log_{10}(\pi/2) \simeq 0.2$] because the outflow is expected to have a bipolar structure such as a jet. We linearly interpolate the observation data between successive observation epochs to depict a continuous colour map. As we have discussed in the previous section, $\Gamma\beta$, $R_{\rm eq}$, and $E_{\rm eq}$ attain minimal values for $\theta = 0$ in the Newtonian (on-axis) branch. Larger values are needed for different viewing angles.

The Newtonian branch is essentially the same as the one found in the previous studies (Cendes et al. 2021; Stein et al. 2021; Matsumoto et al. 2022; Mohan et al. 2022). For brevity, we did not include in our analysis the energies of the hot proton and total non-thermal electrons (in the case of $\nu_{\rm m} < \nu_{\rm a}$) and a possible deviation from the exact equipartition (see BNP13). However, the radius estimate (hence the Lorentz factor) does not change significantly whether these contributions are included. For example, adding the contribution of hot protons increases the total energy by a factor of $\sim$10 (assuming the non-thermal electron energy is $\sim$ 10 per cent of proton energy).

The relativistic branch represents a relativistic jet viewed off-axis disguised as a Newtonian source. With $\beta_{\rm eq,N} \simeq 0.04$, the emission is de-boosted by the Doppler factor of $\delta_{\rm D} \simeq 0.1$ (equation 29). Intriguingly, Mohan et al. (2022) detected a possible superluminal

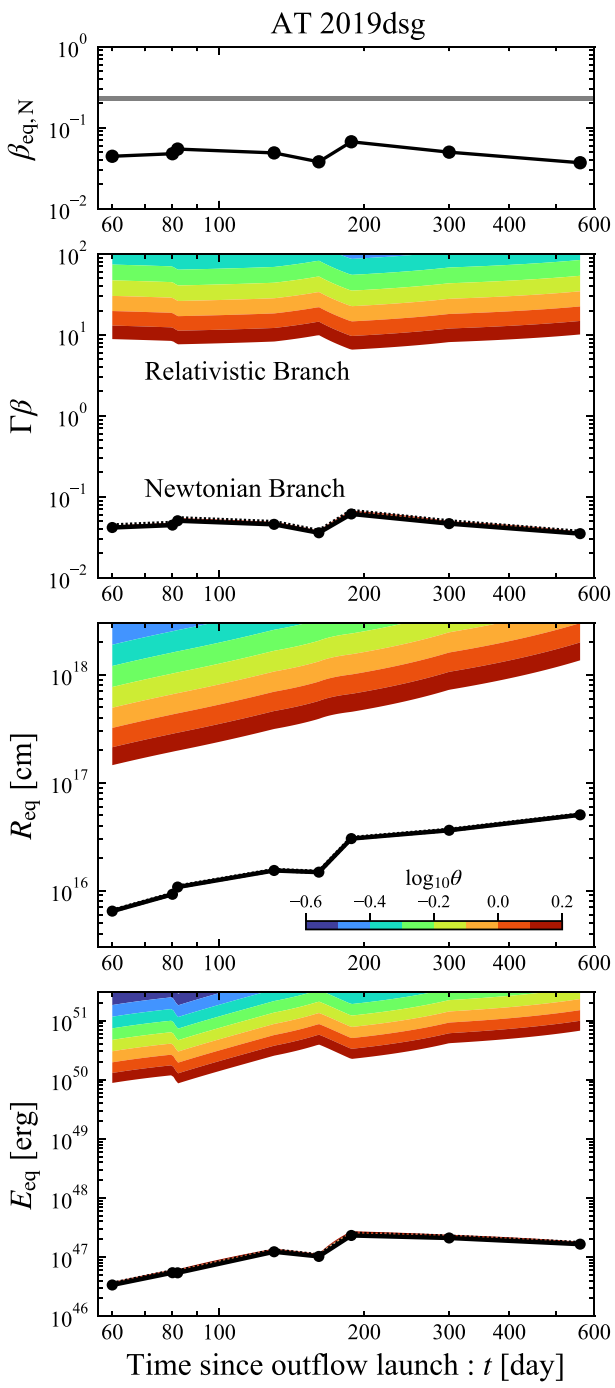

Figure 9. The time evolution of the parameter $\beta_{\rm eq,N}$, four-velocity $\Gamma\beta$, and the equipartition radius $R_{\rm eq}$ and energy $E_{\rm eq}$ for AT 2019dsg. The outflow launching time is set 10 d before the discovery. In the top panel, the grey line shows the critical value of $\beta_{\rm eq,N} = 0.23$ below which the allowed parameter space splits into Newtonian and relativistic branches. Colour contours show the allowed parameter spaces in the second to fourth panels. The black solid and dotted curves show the parameter values for $\theta = 0$ and the contour for the boundary between on- and off-axis ($\theta = \cos^{-1}\beta$). They almost overlap for small $\beta_{\rm eq,N}$. Observables are linearly interpolated to depict the colour map. Note that in the upper regions of all figures, while the angles are very small the solutions are off-axis as $\theta < 1/\Gamma$.

motion of the radio source at AT 2019dsg: $\beta_{\rm VLBI} = 3.2 \pm 2.2$ (1σ confidence level). While the result is not statistically significant, we can use these values and estimate (using the intersection of the trajectories of the minimal energy with $\beta_{\rm eq,N} = 0.04$ (equation 29) and the apparent velocity of $\beta_{\rm VLBI} = 3.2 \pm 2.2$ (equation 44) the corresponding parameters of the system: $\theta \simeq 0.6^{+0.9}_{-0.2}$ and $\Gamma\beta \simeq 50^{+100}_{-40}$ (see Fig. 6). The lowest-energy solution in this branch is realized for $\theta \simeq \pi/2$, $\Gamma \simeq 10$, and $E_{\rm eq}$ increasing from $\sim 10^{50}$ erg to $\sim 10^{51}$ erg. This should be compared with $E_{\rm eq} \simeq 10^{47}$ erg for the Newtonian case. While this energy is much larger than the on-axis case, it is reasonably within the total energy budget of a TDE.

However, the expected time evolution of the jet makes this solution unlikely. The jet should eventually decelerate and become Newtonian. Such a transition occurs only if $\beta_{\rm eq,N} > 0.23$ for which both branches merge. The current observation finds that the peak flux density already started declining $F_{\rm p} \propto t^{-1.2}$ and the peak frequency decreases $\nu_{\rm p} \propto t^{-1}$, which gives $\beta_{\rm eq,N} \propto t^{-0.6}$ (equation 28). Therefore, unless these trends change and either $F_{\rm p}$ increases or $\nu_{\rm p}$ decreases more rapidly, $\beta_{\rm eq,N}$ will continue to decrease monotonically, and the transition to the Newtonian branch will never happen.

4.2 AT 2018hyz

AT 2018hyz (Gomez et al. 2020; Short et al. 2020; van Velzen et al. 2021; Cendes et al. 2022; Hammerstein et al. 2023) shows a relatively bright radio emission $\nu L_\nu \sim 10^{39}$ erg s^{-1} compared to other TDEs, and has a synchrotron self-absorbed spectrum. A peculiar feature is the delayed onset of the radio flare at ∼800 d after the optical discovery (see also Horesh et al. 2021a,b; Perlman et al. 2022; Sfaradi et al. 2022, for possible other events). Cendes et al. (2022) carried out an (on-axis) equipartition analysis and rejected the possibility that the outflow is launched at the time of the optical discovery because it requires a non-monotonic velocity evolution. Their preferred solution is that the outflow producing the radio emission was launched 750 d after the discovery with an almost constant velocity $\beta \simeq 0.2$ (spherical geometry) or $\beta \simeq 0.6$ (jet geometry with $\theta_{\rm j} = 10^\circ \simeq 0.17$).

We examine this event[7] assuming that the outflow is launched at approximately the same time as the optical discovery, i.e. roughly at the same time as the TDE. Fig. 10 depicts our result. Like in AT 2019dsg, $\beta_{\rm eq,N} < 0.23$, and the possible range of quantities is split into two branches. Our results for the Newtonian branch are consistent with those of Cendes et al. (2022) except for the correction to the energy as discussed above.

We find that the radio emission may be produced by a relativistic jet viewed off-axis as first studied by Giannios & Metzger (2011).[8] For a viewing angle of $\theta \simeq \pi/2$ (brown coloured stripe in Fig. 10), the outflow has a slowly decreasing Lorentz factor from $\Gamma \simeq 8$ to $\simeq 5$ with a Doppler factor of $\delta_{\rm D} \simeq 0.1$ to 0.2. The equipartition energy is also weakly increasing from $E_{\rm eq} \simeq 2 \times 10^{51}$ erg to $\simeq 3 \times 10^{51}$ erg. In this solution, an on-axis observer would see a bright emission from this jet. Using the quantities of $\delta_{\rm D} \simeq 0.2$, $\Gamma \simeq 5$, and spectrum at 1251 d, we estimate the on-axis radio luminosity at 5 GHz of $\nu L_\nu \simeq 10^{42}$ erg s^{-1}, which would be observed at 20 d after the disruption.

[7]Following Cendes et al. (2022), we do not include the data point at 1282 d after the discovery.

[8]Cendes et al. (2022) exclude an off-axis jet arguing that such a scenario predicts a slowly rising flux $F_\nu \propto t^3$. However, this is not necessarily the case as shown in e.g. van Eerten, Zhang & MacFadyen (2010), and Hotokezaka & Piran (2015).

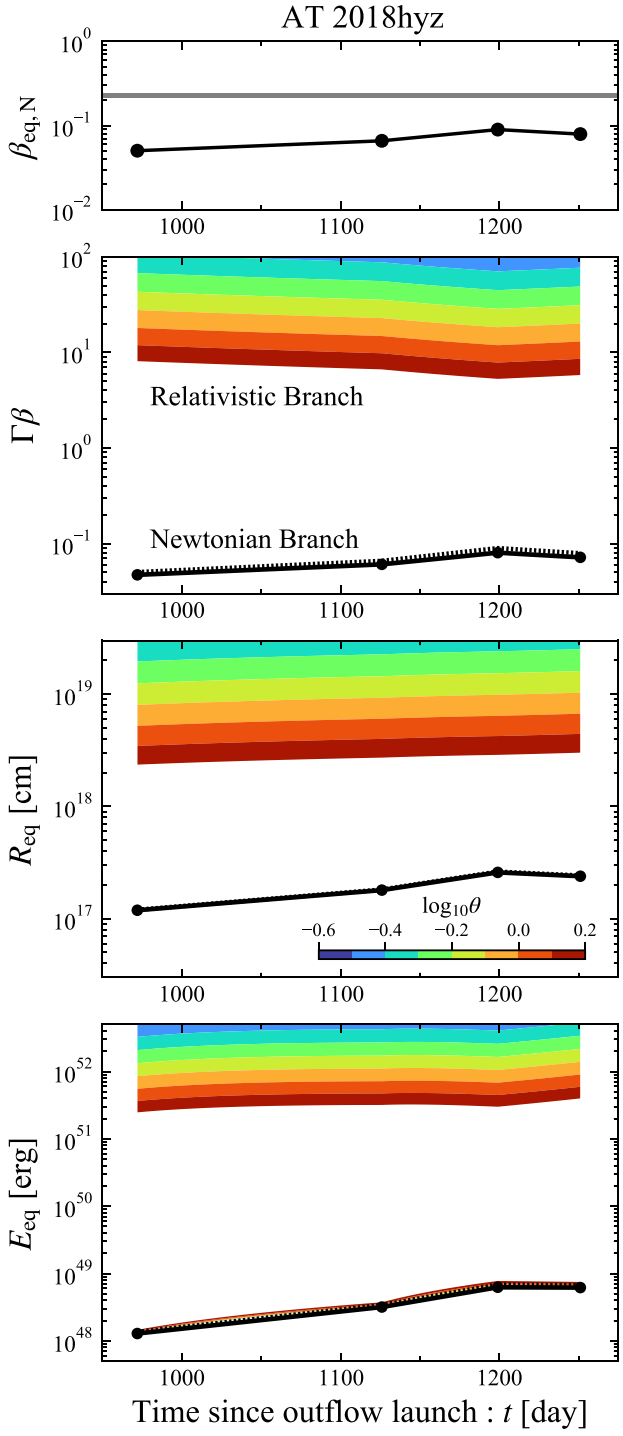

Figure 10. The same as Fig. 9 but for AT 2018hyz. The outflow launching time is set as the time of discovery.

This is about 10 times larger than the jetted TDE Swift J1644+25 (Zauderer et al. 2011; Berger et al. 2012) but comparable to Swift J2058+05 (Brown et al. 2017 and see fig. 1 in Alexander et al. 2020).

The off-axis jet's energetics is directly estimated using the CNM density. Fig. 11 depicts the CNM density profiles reconstructed for both on-axis (Newtonian, black curve) and off-axis (relativistic, brown to orange coloured curves) solutions by using equation (45). The density for the on-axis case is consistent with that of Cendes et al. (2022) within a factor of 2. The off-axis solution has a density profile

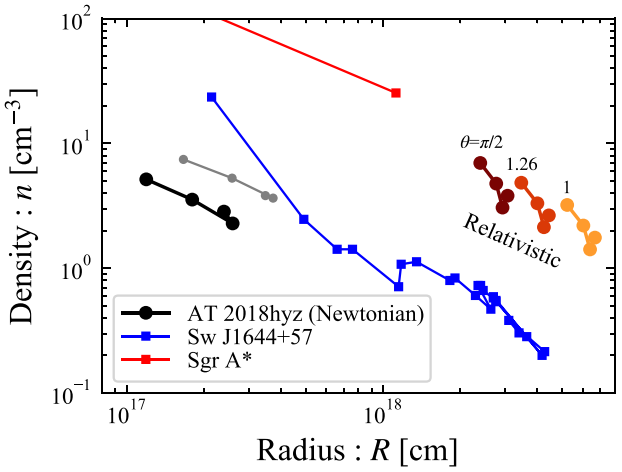

Figure 11. CNM density profile reconstructed by our equipartition analysis for AT 2018hyz. The black curve shows the density profile for the on-axis Newtonian branch. The brown to yellow ones show profiles for off-axis relativistic branches with different viewing angles [$\theta = \pi/2$, 1.26($\simeq 10^{0.1}$), and 1 from left to right]. The grey and blue curves denote the profiles of AT 2018hyz calculated by Cendes et al. 2022 and of Swift J1644+57 Eftekhari et al. 2018. The red curve shows the profile for our Galactic center (Baganoff et al. 2003; Gillessen et al. 2019).

about 10 times larger than that of the jetted TDE Swift J1644+57 (Eftekhari et al. 2018),[9] but it is similar to that of our Galactic center (Sgr A∗) if it extends with the same slope. Since the off-axis viewed jet is decelerating, the jet energy is estimated by the total energy of the swept-up CNM. The swept-up mass is obtained by

$$M_{\rm swept} \sim m_{\rm p} n \frac{\pi}{\Gamma^2}\frac{R^3}{3} \simeq 3\times10^{-3}\,{\rm M}_\odot \left(\frac{n}{3\,{\rm cm}^{-3}}\right)\left(\frac{R}{3\times10^{18}\,{\rm cm}}\right)^3\left(\frac{\Gamma}{5}\right)^{-2}. \quad (46)$$

Therefore, the total kinetic energy of the jet (including the proton's energy) is $E_{\rm kin} \simeq \Gamma^2 M_{\rm swept} c^2 \simeq 10^{53}$ erg. The energy of the emitting electron ($E_{\rm eq} \simeq 3\times10^{51}$ erg) is $\simeq 3$ per cent of the total jet energy. The total jet energy, 10^{53} erg, is about 10 times larger than that of jetted TDEs implied by X-ray observations ($\sim 10^{52}$ erg; Bloom et al. 2011; Burrows et al. 2011; Levan et al. 2011; Cenko et al. 2012; Brown et al. 2015; Pasham et al. 2015), but within the range of the energies required by several radio modellings for Swift 1644+57 ($\sim 10^{53}$ erg; Barniol Duran & Piran 2013; Mimica et al. 2015; Generozov et al. 2017), and recently reported jetted TDE candidate AT 2022cmc (Matsumoto & Metzger 2023).

This off-axis scenario can be tested as $\beta_{\rm eq,N}$ has to increase to allow a late-time transition to the on-axis Newtonian branch within this solution. This requires that either the peak flux increases or the peak frequency decreases. Unlike AT 2019dsg, at the latest observation, the peak flux density of AT 2018hyz is increasing as $F_{\rm p} \propto t^5$ (the peak frequency is relatively stable) and hence $\beta_{\rm eq,N}$ increases $\propto t^{1.4}$. Within this model, the peak flux will continue to increase (or peak frequency will start decreasing). Using the evolution of $\Gamma \propto t^{-1.9}$

[9]We multiply a numerical factor of four by the densities obtained by Eftekhari et al. (2018) and Cendes et al. (2022). They introduced this factor to correct the shock compression, which is, however, not needed to estimate the CNM profile (Matsumoto et al. 2022).

implied in Fig. 10,[10] we estimate that the jet becomes Newtonian at $\simeq 3000$ d after the disruption, and the light curve will peak around that time.

VLBI observations will be able to test the off-axis scenario directly. In the off-axis scenario, the relativistic jet travels roughly perpendicularly to our line of sight at the speed of light. For the distance of $\simeq 200$ Mpc to AT 2018hyz, such a source moves at $\simeq 0.3$ mas yr^{-1} on the sky plane. Given that the radio flux of $\simeq 3$–10 mJy at the last epoch, which is brighter than the radio afterglow of GRB 170817A, ~ 0.1 mJy, for which a superluminal motion was detected (Mooley et al. 2018; Ghirlanda et al. 2019), given that the radio signal is rising we expect that VLBI observation will give an interesting constraint on the off-axis scenario. By the time of the expected peak at $\simeq 3000$ d, the distance from the image has traversed should be $\simeq 2.4$ mas. Detection of such a motion will be a 'smoking gun' for the off-axis scenario. Alternatively, a null result will rule it out. If this scenario is confirmed, this jet's implied very large energy will have interesting implications for the central engines in TDEs.

5 SUMMARY

We generalized the equipartition method of BNP13 for an arbitrary viewing angle θ. As found by BNP13, the introduction of relativistic motion implies that the total energy inferred from the equipartition analysis can be arbitrarily small (for $\theta = 0$). This is because with a higher Lorentz factor, the observed region becomes smaller and smaller, and hence it contains less and less energy. In this sense, the estimated equipartition energy does not reflect the system's actual total energy (presumably broader than Γ^{-1}). Thus, simply minimizing the energy does not give a solution.

Following BNP13, we impose another condition relating the radius and the observation time (equation 26 or 27) to obtain the equipartition radius and energy. Unlike the on-axis scenario, the Lorentz factor cannot be determined uniquely in this case. It becomes degenerate with the viewing angle along the minimal energy trajectory (equation 29, see also Fig. 6) that is characterized by a velocity parameter $\beta_{\rm eq,N}$. The possible solutions are divided into on-axis and off-axis branches. The latter branch always has larger Lorentz factor and the equipartition radius and energy than those in the on-axis branch. For a velocity parameter smaller than a critical value $\beta_{\rm eq,N} \lesssim 0.23$, the trajectory is split into these two (on-axis Newtonian and off-axis relativistic) branches. The off-axis relativistic branch implies that an apparent Newtonian radio source can be a relativistic source viewed off-axis.

The degeneracy between the Lorentz factor and viewing angle implies that an observed radio signal could have very different interpretations. To demonstrate this, we analysed two radio TDEs, AT 2019dsg and AT 2018hyz. Both are 'apparently' Newtonian radio TDEs with $\beta_{\rm eq,N} \lesssim 0.23$. However, they could be indeed produced by a relativistic jet viewed off-axis. For these objects, long-term monitoring or, equivalently, the evolution of $\beta_{\rm eq,N}$ is critical to distinguish whether they are produced by a Newtonian outflow or relativistic jet. If the radio emitter is a jet and it evolves into the Newtonian branch, $\beta_{\rm eq,N}$ should increase to above the critical value $\beta_{\rm eq,N} \gtrsim 0.23$. Current observations of AT 2019dsg find a decreasing velocity parameter, making the possibility of a jet unlikely.

[10]This evolution may be consistent with the evolution of Γ after a jet break for an off-axis observer (e.g. De Colle et al. 2012).

The situation is different for AT 2018hyz, which involves a delayed radio flare occurring more than 2 yr after the optical discovery. For this event, $\beta_{\rm eq,N}$ is increasing, which suggests that an off-axis relativistic jet is an intriguing alternative explanation for the origin of delayed radio flares. More importantly, this scenario can be tested as it predicts an increasing radio flux over the next few years as well as a motion of the radio source that can be measured using VLBI. Further observations of this event, such as exploration of flux and peak luminosity that determines $\beta_{\rm eq,N}$ and VLBI observations of the centroid motion, could distinguish between this solution and the alternative late launch of an outflow. Furthermore, the solution requires a significant jet energy $\sim 10^{53}$ erg which is comparable to estimates, based on the radio emission, of the total jet energy of Swift J1644+57 (Barniol Duran & Piran 2013; Mimica et al. 2015; Generozov et al. 2017). This will have remarkable implications for our understanding of TDE's central engines if verified.

The estimated event rate of jetted TDEs is highly uncertain but consistent with our off-axis scenario for AT 2018hyz. While the rate of on-axis jetted events is poorly constrained, $\sim 10^{-2}$ Gpc^{-3} yr^{-1} (Alexander et al. 2020; De Colle & Lu 2020), taking a beaming fraction of $f_{\rm beam} \sim 10^{-2}$ and total TDE rate of $\sim 10^{2}$–10^{3} Gpc^{-3} yr^{-1} (van Velzen 2018; Lin et al. 2022), the fraction of jetted TDE is estimated to be $\sim 10^{-3}$ to 10^{-2}. Since the total number of detected TDE candidates is $\sim$100 (Gezari 2021; Sazonov et al. 2021; Hammerstein et al. 2023), a few optically detected events can harbour off-axis jets, which are potentially detected as a delayed radio emission. Note that while a jet that points toward us is much easier to detect, it is much more likely that a jet will point elsewhere than toward us.

Our analysis stresses the importance of VLBI observation of late-time radio images of TDEs. Such observations are possibly the best way to reveal the existence of relativistic jets in these systems. The optical signals on which most events are triggered are roughly isotropic, having no preference for on-axis configurations. As such, we will most likely capture TDE jets pointing off-axis away from us. Superluminal motion is a natural consequence if these jets are relativistic.

ACKNOWLEDGEMENTS

We thank Kunihito Ioka and an anonymous referee for useful comments. This work is supported in part by JSPS Overseas Research Fellowships (TM) and by ERC advanced grants 'TReX' and 'MultiJets' (TP).

DATA AVAILABILITY

The data underlying this article will be shared on reasonable request to the corresponding author.

REFERENCES

Alexander K. D., Berger E., Guillochon J., Zauderer B. A., Williams P. K. G., 2016, ApJ, 819, L25
Alexander K. D., van Velzen S., Horesh A., Zauderer B. A., 2020, Space Sci. Rev., 216, 81
Baganoff F. K. et al., 2003, ApJ, 591, 891
Barniol Duran R., Piran T., 2013, ApJ, 770, 146
Barniol Duran R., Nakar E., Piran T., 2013, ApJ, 772, 78
Berger E., Zauderer A., Pooley G. G., Soderberg A. M., Sari R., Brunthaler A., Bietenholz M. F., 2012, ApJ, 748, 36
Bloom J. S. et al., 2011, Science, 333, 203

Brown G. C., Levan A. J., Stanway E. R., Tanvir N. R., Cenko S. B., Berger E., Chornock R., Cucchiaria A., 2015, MNRAS, 452, 4297
Brown J. S., Holoien T. W. S., Auchettl K., Stanek K. Z., Kochanek C. S., Shappee B. J., Prieto J. L., Grupe D., 2017, MNRAS, 466, 4904
Bruni G., O'Connor B., Matsumoto T., Troja E., Piran T., Piro L., Ricci R., 2021, MNRAS, 505, L41
Burrows D. N. et al., 2011, Nature, 476, 421
Cannizzaro G. et al., 2021, MNRAS, 504, 792
Cendes Y., Alexander K. D., Berger E., Eftekhari T., Williams P. K. G., Chornock R., 2021, ApJ, 919, 127
Cendes Y. et al., 2022, ApJ, 938, 28
Cenko S. B. et al., 2012, ApJ, 753, 77
Chevalier R. A., 1998, ApJ, 499, 810
De Colle F., Lu W., 2020, New Astron. Rev., 89, 101538
De Colle F., Guillochon J., Naiman J., Ramirez-Ruiz E., 2012, ApJ, 760, 103
Dermer C. D., Menon G., 2009, High Energy Radiation from Black Holes: Gamma Rays, Cosmic Rays, and Neutrinos. Princeton Univ. Press, Princeton, NJ
Eftekhari T., Berger E., Zauderer B. A., Margutti R., Alexander K. D., 2018, ApJ, 854, 86
Generozov A., Mimica P., Metzger B. D., Stone N. C., Giannios D., Aloy M. A., 2017, MNRAS, 464, 2481
Gezari S., 2021, ARA&A, 59, 21
Ghirlanda G. et al., 2019, Science, 363, 968
Giannios D., Metzger B. D., 2011, MNRAS, 416, 2102
Gillessen S. et al., 2019, ApJ, 871, 126
Gomez S. et al., 2020, MNRAS, 497, 1925
Granot J., Panaitescu A., Kumar P., Woosley S. E., 2002, ApJ, 570, L61
Hammerstein E. et al., 2023, ApJ, 942, 9
Horesh A., Cenko S. B., Arcavi I., 2021a, Nature Astron., 5, 491
Horesh A., Sfaradi I., Fender R., Green D. A., Williams D. R. A., Bright J. S., 2021b, ApJ, 920, L5
Hotokezaka K., Piran T., 2015, MNRAS, 450, 1430
Ioka K., Nakamura T., 2019, MNRAS, 487, 4884
Krolik J., Piran T., Svirski G., Cheng R. M., 2016, ApJ, 827, 127
Lee C.-H., Hung T., Matheson T., Soraisam M., Narayan G., Saha A., Stubens C., Wolf N., 2020, ApJ, 892, L1
Levan A. J. et al., 2011, Science, 333, 199
Lin Z., Jiang N., Kong X., Huang S., Lin Z., Zhu J., Wang Y., 2022, ApJ, 939, L33
Margutti R., Chornock R., 2021, ARA&A, 59, 155
Matsumoto T., Metzger B. D., 2023, preprint (arXiv:2301.11939)
Matsumoto T., Piran T., 2021, MNRAS, 507, 4196
Matsumoto T., Nakar E., Piran T., 2019a, MNRAS, 483, 1247
Matsumoto T., Nakar E., Piran T., 2019b, MNRAS, 486, 1563
Matsumoto T., Piran T., Krolik J. H., 2022, MNRAS, 511, 5085
Mimica P., Giannios D., Metzger B. D., Aloy M. A., 2015, MNRAS, 450, 2824
Mohan P., An T., Zhang Y., Yang J., Yang X., Wang A., 2022, ApJ, 927, 74
Mooley K. P. et al., 2018, Nature, 561, 355
Nakar E., Piran T., 2002, MNRAS, 330, 920
Pacholczyk A. G., 1970, Radio astrophysics. Nonthermal processes in galactic and extragalactic sources. Freeman & Co., San Francisco
Pasham D. R. et al., 2015, ApJ, 805, 68
Perlman E. S. et al., 2022, ApJ, 925, 143
Petropoulou M., Dermer C. D., 2016, ApJ, 825, L11
Rossi E., Lazzati D., Rees M. J., 2002, MNRAS, 332, 945
Sari R., Piran T., Narayan R., 1998, ApJ, 497, L17
Sazonov S. et al., 2021, MNRAS, 508, 3820
Scott M. A., Readhead A. C. S., 1977, MNRAS, 180, 539
Sfaradi I., Horesh A., Fender R., Green D. A., Williams D. R. A., Bright J., Schulze S., 2022, ApJ, 933, 176
Short P. et al., 2020, MNRAS, 498, 4119
Stein R. et al., 2021, Nature Astron., 5, 510
Totani T., Panaitescu A., 2002, ApJ, 576, 120
van Eerten H., Zhang W., MacFadyen A., 2010, ApJ, 722, 235
van Velzen S., 2018, ApJ, 852, 72
van Velzen S. et al., 2021, ApJ, 908, 4
Winter W., Lunardini C., 2021, Nature Astron., 5, 472
Yalinewich A., Steinberg E., Piran T., Krolik J. H., 2019, MNRAS, 487, 4083
Zauderer B. A. et al., 2011, Nature, 476, 425
Zauderer B. A., Berger E., Margutti R., Pooley G. G., Sari R., Soderberg A. M., Brunthaler A., Bietenholz M. F., 2013, ApJ, 767, 152
Zdziarski A. A., 2014, MNRAS, 445, 1321

APPENDIX A: DERIVATION OF PEAK FLUX $F_{\rm P}$

We derive equations (3) and (6). A photon with a frequency ν' at the rest frame of the emitting region is observed as a photon with a frequency of

$$\nu_{\rm obs} = \frac{\delta_{\rm D}\nu'}{1+z}\ , \tag{A1}$$

by the Doppler boost and redshift effect. Let us consider an emitting object whose luminosity distributes over the solid angle at the lab frame by $\mathrm{d}L_\nu/\mathrm{d}\Omega$. The observed flux is given by

$$F_{\nu_{\rm obs}} = \frac{(1+z)}{d_{\rm L}^2}\frac{\mathrm{d}L_\nu}{\mathrm{d}\Omega}\ . \tag{A2}$$

When the emitting region is optically thin, the luminosity distribution is given by the volume and emissivity:

$$\frac{\mathrm{d}L_\nu}{\mathrm{d}\Omega} = j_\nu V = \delta_{\rm D}^3 j'_{\nu'} V'\ , \tag{A3}$$

where we have transformed the quantities in the lab frame and rest frame, $j_\nu = (\nu/\nu')^2 j'_{\nu'}$, $V = \delta_{\rm D} V'$, and $\nu = \delta_{\rm D}\nu'$. Combining equations (A2) and (A3), the observed flux is given by

$$F_{\nu_{\rm obs}} = \frac{(1+z)\delta_{\rm D}^3}{d_{\rm L}^2} j'_{\nu'} V'\ . \tag{A4}$$

This corresponds to equation (5.42) of Dermer & Menon (2009). By assuming the emission is isotropic at the rest frame and using $j'_{\nu'}V' = P'_{\nu'}N_{\rm e}/4\pi$ where $P'_{\nu'} = \sqrt{3}q_{\rm e}^3 B/m_{\rm e}c^2$ is the synchrotron emissivity, we have equation (3). When the source is optically thick, the luminosity distribution is given by the intensity and surface area:

$$\frac{\mathrm{d}L_\nu}{\mathrm{d}\Omega} = I_\nu A = \delta_{\rm D}^3 I'_{\nu'} A\ , \tag{A5}$$

where we used the transformation of $I_\nu = (\nu/\nu')^3 I'_{\nu'}$. Finally, we have the observed flux of

$$F_{\nu_{\rm obs}} = \frac{(1+z)\delta_{\rm D}^3}{d_{\rm L}^2} I'_{\nu'} A\ . \tag{A6}$$

When the system is optically thick, the intensity is given by the Planck function. In particular, if the observed frequency is smaller than the peak frequency, the Rayleigh–Jeans formula gives equation (6).

APPENDIX B: NARROW JET GEOMETRY

If a jet can keep its half-opening angle $\theta_{\rm j}$ even after a significant deceleration $\Gamma \ll 1/\theta_{\rm j}$, we have to take into account the geometrical effect by modifying the factors of

$$f_{\rm A} = f_{\rm V} = (\Gamma\theta_{\rm j})^2\ . \tag{B1}$$

The procedure to obtain the equipartition quantities is the same as that in the case of $f_{\rm A} = f_{\rm V} = 1$, and we have

$$R_{\rm eq} = R_{\rm eq,Nj}\Gamma^{1/17}\delta_{\rm D}^{-7/17}\ , \tag{B2}$$

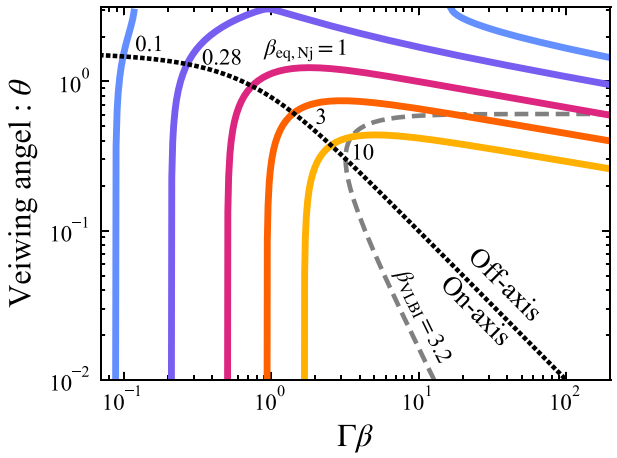

Figure B1. The same as Fig. 6 but for a narrow jet geometry.

$$R_{\rm eq,Nj} \simeq 1.6\times10^{18}\,{\rm cm}\left[\frac{F_{\rm p,mJy}^{\frac{8}{17}}d_{\rm L,28}^{\frac{16}{17}}\eta^{\frac{35}{51}}}{\nu_{\rm p,10}(1+z)^{\frac{25}{17}}}\right]\left(\frac{\theta_{\rm j}}{0.1}\right)^{-16/17},$$
$$E_{\rm eq} = E_{\rm eq,Nj}\Gamma^{11/17}\delta_{\rm D}^{-43/17}, \tag{B3}$$
$$E_{\rm eq,Nj} \simeq 1.4\times10^{50}\,{\rm erg}\left[\frac{F_{\rm p,mJy}^{\frac{20}{17}}d_{\rm L,28}^{\frac{40}{17}}\eta^{\frac{15}{17}}}{\nu_{\rm p,10}(1+z)^{\frac{37}{17}}}\right]\left(\frac{\theta_{\rm j}}{0.1}\right)^{-6/17}.$$

Here the Newtonian radius $R_{\rm eq,Nj}$ and energy $E_{\rm eq,Nj}$ are given by replacing $f_{\rm A}$ and $f_{\rm V}$ with $\theta_{\rm j}^2$ in the original equations, (17) and (19). Now the energy (equation 22) and minimal energy trajectory (equation 29) are modified by

$$e(r,\Gamma,\theta) = \Gamma^{\frac{11}{17}}\delta_{\rm D}^{-\frac{43}{17}}\left[\frac{11}{17}\left(\frac{r}{\Gamma^{\frac{1}{17}}\delta_{\rm D}^{-\frac{7}{17}}}\right)^{-6}+\frac{6}{17}\left(\frac{r}{\Gamma^{\frac{1}{17}}\delta_{\rm D}^{-\frac{7}{17}}}\right)^{11}\right], \tag{B4}$$

$$\delta_{\rm D} = \left(\frac{\beta_{\rm eq,Nj}}{\beta}\right)^{17/24}\Gamma^{-2/3}, \tag{B5}$$

where

$$\beta_{\rm eq,Nj} \equiv \frac{(1+z)R_{\rm eq,Nj}}{ct} \simeq 6.3\left[\frac{F_{\rm p,mJy}^{\frac{8}{17}}d_{\rm L,28}^{\frac{16}{17}}\eta^{\frac{35}{51}}}{\nu_{\rm p,10}(1+z)^{\frac{8}{17}}}\left(\frac{t}{100\,{\rm d}}\right)^{-1}\right]\left(\frac{\theta_{\rm j}}{0.1}\right)^{-16/17}. \tag{B6}$$

Figs B1 and B2 show the same figures as Figs 6 and 7 but for a narrow jet geometry. The qualitative feature does not change.

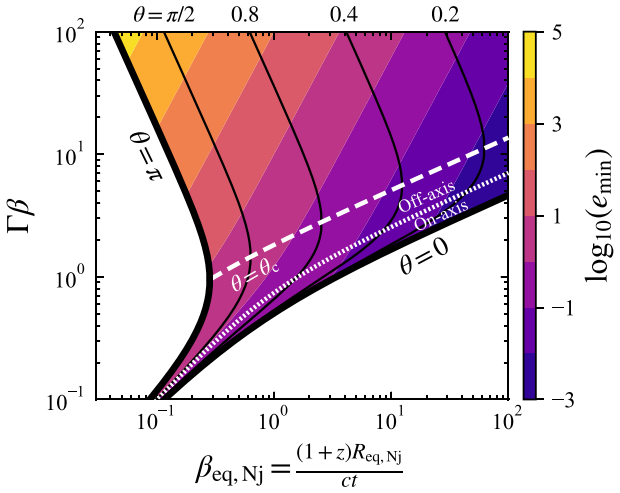

Figure B2. The same as Fig. 7 but for a narrow jet geometry.

This paper has been typeset from a TEX/LATEX file prepared by the author.